Photoacoustics 19 (2020) 100188

Contents lists available at ScienceDirect

Photoacoustics

journal homepage: www.elsevier.com/locate/pacs

Resolution-matched reflection mode photoacoustic microscopy and optical coherence tomography dual modality system

Xiaoyi Zhu, Zhiyu Huang, Ziyuan Li, Wenzhao Li, Xi Liu, Zhaolong Chen, Jian Tian, Changhui Li*

Department of Biomedical Engineering, College of Engineering, Peking University, Beijing, 100871, China

ARTICLE INFO

Keywords:
Photoacoustic imaging
Optical coherence tomography
Detection
Multiple imaging

ABSTRACT

Photoacoustic microscopy (PAM) and optical coherence tomography (OCT) are sensitive to optical absorption and scattering characteristics, respectively. As such, the integration of these two modalities in order to combine important complementary information has garnered much attention. Due to the relatively low axial resolution of PAM, PAM and OCT dual modality systems generally have a large resolution gap, especially for reflection mode systems. In this study, based on a wide-band transparent pure-optical ultrasonic detector, we developed a dual modality system (PAM-OCT system) in which PAM has a similar spatial resolution (*i.e.* several micrometers in both the lateral and axial directions) to OCT. In addition, due to the optical transparency advantage, the integrated system works in reflection mode, which is ideal for *in vivo* biomedical imaging. We successfully imaged the skin of a mouse hindlimb, which cannot be done by a transmission mode dual modality system. Our work demonstrates this dual modality system has potential in biomedical studies with complementary imaging contrasts.

1. Introduction

Photoacoustic microscopy (PAM), which detects ultrasonic signals after the tissue absorbs photon energy, is highly sensitive to optical absorption [1] while optical coherence tomography (OCT) is more sensitive to optical scattering [2]. Both microscopic imaging methods have similar imaging depths of up to a few millimeters. Therefore, work towards integrating these two complementary modalities to image multiple tissues, including skin, retina, cortex, ovarian, and embryo tissue, has gained much attention [3–7].

In a PAM-OCT system, the lateral resolutions of these two modalities are all determined by optical focusing, which can feasibly be aligned to be approximately equal. However, unlike OCT whose axial resolution is primarily determined by the bandwidth of the low-coherence light source, the axial resolution of PAM depends on both the detector's bandwidth and ultrasound attenuation through the source to the detector. The typical axial resolution of OCT is less than 10 μm. To achieve a similar resolution, a PAM system needs to be able to detect ultrasonic signals over 100 MHz. In some cases, such as non-invasive retinal imaging, the distance from the source (*i.e.* retina) to the detector is so great that the high-frequency ultrasonic signal can hardly survive, therefore making high-axial resolution for PAM inapplicable, while simultaneously for many other imaging targets, including skin, zebrafish, embryo, *etc.*, a high-frequency photoacoustic (PA) signal can effectively penetrate the tissue and reach the detector. Therefore, it is desirable to have similar spatial resolution in both OCT and PAM for these studies.

There are two major types of ultrasonic detector in PAM, piezoelectric material-based transducers and pure optical-based ultrasonic detectors. Although various kinds of piezoelectric material-based ultrasound transducers are commercially available and widely used, it is challenging to manufacture transducers with both high sensitivity and an extremely wide bandwidth (over 100 MHz) [8]. Besides that, the opacity of the piezoelectric-based transducer also hinders the integration of PAM with OCT if the transducer is too close to the target to detect high-frequency ultrasonic waves effectively (especially for reflection mode). C. Zhang et al. reported a PAM-OCT system with a commercial piezoelectric-material transducer with a central frequency over 100 MHz, but that system works in the transmission mode [9]. In recent years, tremendous strides have been made in pure-optical ultrasonic detection methods, including low-coherence interferometry (Michelson [10] or Mach–Zehnder [11]), surface displacement interferometry [12], full-field speckle interferometry [13], surface plasmon resonance detection [14], Fabry–Perot interferometry [15], optical micro-ring resonance [16], graphene-based PAM [17], and polarization-dependent reflection ultrasonic detection (PRUD) [18].The Fabry–Perot interferometry and low-coherence interference have already been successfully integrated with OCT [10,11,15], but the axial resolutions of PA modality in these systems are all many times of

* Corresponding author.
E-mail address: chli@pku.edu.cn (C. Li).

https://doi.org/10.1016/j.pacs.2020.100188
Received 9 December 2019; Received in revised form 22 April 2020; Accepted 29 April 2020
Available online 03 June 2020

Table 1
Comparison of axial resolutions from typical reported works.

Methods	Axial resolution (μm)	
	OCT	PA
Fabry–Perot interferometry [3,7,15,19]	5–8	20–40
Low-coherence interferometry [10,11,20,21]	8–13	20–60

magnitude larger than that of OCT, as listed in Table 1. The resolution gap is primarily due to the limited bandwidth of the equipped pure optical ultrsound detection systems. Among those reported pure-optical methods, PRUD and micro-ring resonance can both be made optically transparent and to operate with a bandwidth over 100 MHz, thereby having the potential to achieve an omnidirectional resolution-matched PAM-OCT system.

In this study, we explore the integration of PRUD with OCT. The principle of PRUD is that when acoustic waves reach the liquid–glass interface, the acoustic pressure changes the relative refractive index of the two media, leading to perturbations in the reflectance of the optical probe beam in glass, and a small intensity difference between two polarization components of the same probe beam (detected based on a balanced detection method). More details of PRUD can be found in [18]. PRUD achieves an ultra-broad frequency response from almost 0–137.2 MHz (−6 dB). In this work, we integrate PRUD with a spectral domain OCT (SD-OCT) system. The measured axial resolutions of PAM and OCT in our dual modality system are 8 and 7.6 μm, respectively.

2. Experimental setup

Fig. 1 shows the schematic of the PAM-OCT system. The PAM subsystem is based on a PRUD system that uses a continuous He-Ne laser (25-LHP-991-230, Melles Griot; wavelength, 632.8 nm; power, 9 mW; mode, > 90 % TEM_{00}; beam diameter, ~1.02 mm) as the probe beam. The probe laser is tuned to be circularly polarized by a quarter-wave plate (WPQ05M-633, Thorlabs). Then, it is weakly focused through a convex lens onto the bottom surface of the customized trapezoid prism (UV fused silica, length = 25 mm, height = 10 mm, base width = 21.23 mm, top width = 20.93 mm). The reflected probe beam is then collected by another convex lens, separated by a polarization beam splitter (PBS201, Thorlabs) into *p*-wave and *s*-wave, and detected by a high-frequency balanced detector (PDB450A, Thorlabs). The signal from the balanced amplified photodetector is recorded by a digital oscilloscope (DPO 3034, Tektronix) with 2.5 GHz sampling rate or an acquisition card (CS-1422, Gage) with 200 MHz sampling rate. The repetition rate of the oscilloscope for acquiring data is low (less than 10 Hz), so we used the acquisition card to do fast-triggered data acquisition for imaging a large area. The PA excitation source was a 532 nm Nd:YAG pulsed laser with 1 kHz repetition rate (Elforlight SPOT-10−100-532; pulse width < 1.8 ns; pulse energy, 3.8 μJ; mode, TEM_{00}, M 2 < 1.1; beam diameter, ~1 mm), which passed down through a dichroic mirror (FF49-SDi01, Semrock), an objective lens (NA = 0.1, Plan N Infinity, 4 ×, Olympus), and a transparent trapezoid prism, and then focused on the sample. The interval between the prism and the sample was filled with deionized (DI) water as the ultrasonic coupling medium. We chose a 1 kHz repetition rate for the laser because of the limited scanning speed of the customized stepping motor control stage (5 mm/s).

The SD-OCT subsystem used a broadband super-luminescent diode (IPSDS0804, Inphenix) with a central wavelength of 840 nm and a full width at half-maximum bandwidth (FWHM) of 30 nm. The light was separated into the reference beam and sample beam by a 2 × 2 fiber coupler (TW850R5A2, Thorlabs). The sample beam was first reflected from a dichroic mirror that allowed the PA excitation light to pass through, and then focused on the sample after passing through the same objective lens and the same prism as were used in PRUD. The light was a little dispersed after passing through the prism. We corrected the dispersion through post-processing [22]. The light energy loss of the PAM and OCT was about 5% after passing through the prism. The reflected light from the two beams interfered with one another before being diffracted by a high-performance optical grating (Wasatch Photonics) and detected by a linear CCD (AT71YSM2CL2014, Teledyne) with a 28 kHz line scan rate.

Owing to the transparent prism, we can combine the PA excitation laser with the OCT light to perform reflection mode imaging. This epi-illumination and detection configuration is crucial for *in vivo* animal studies. We used a microcontroller board with an STM32 F series MCU to synchronize the triggers for four instruments: the pulsed laser to

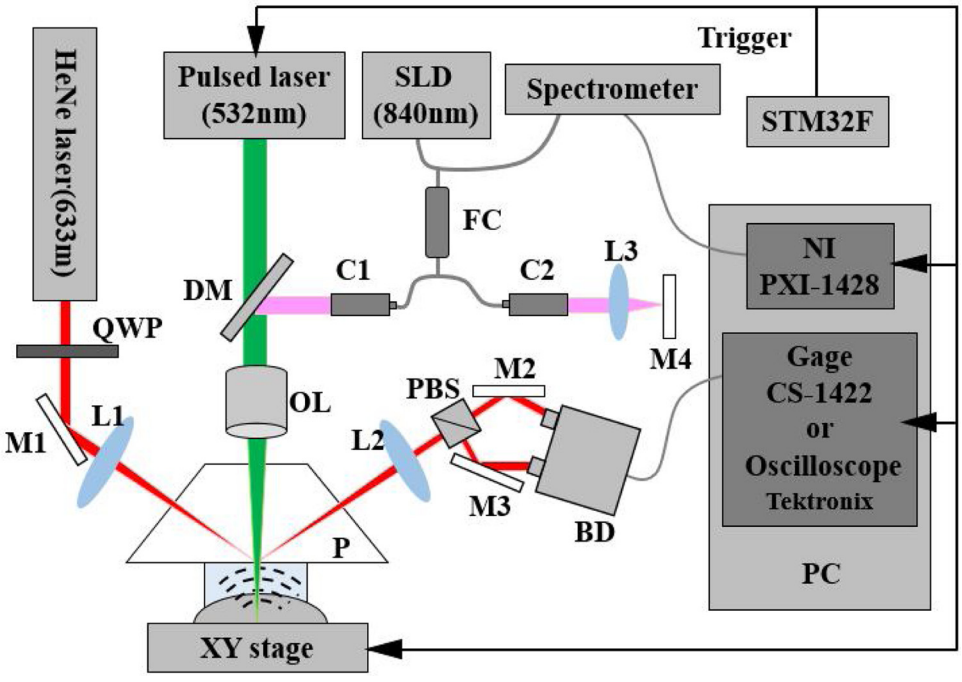

Fig. 1. Schematic of the PAM-OCT imaging system. SLD, super-luminescent diode; QWP, quarter-wave plate; DM, dichroic mirror; C1; 2, collimator; FC, fiber coupler; L1; 2; 3, lens; M1; 2; 3; 4, mirror; OL, objective lens; PBS, polarization beam splitter; P, prism; BD, balanced detector; STM32 F, a family of 32-bit microcontroller integrated circuits by STMicroelectronics.

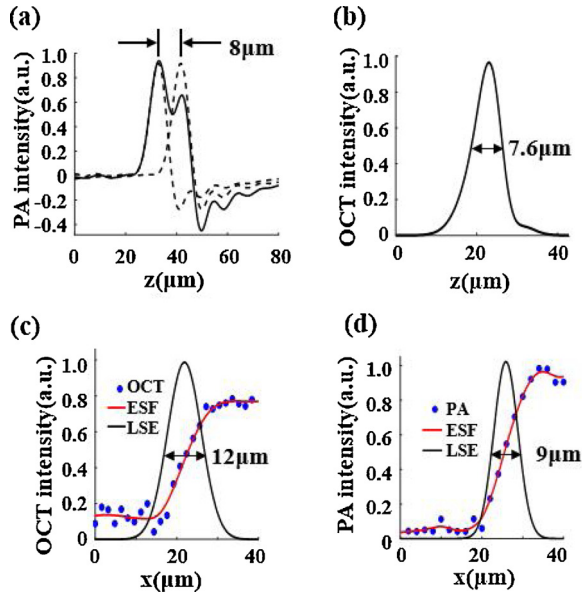

Fig. 2. Spatial resolution of the PAM-OCT system. (a) Axial resolution of PAM quantified using the shift-and-sum method; (b) axial resolution of SD-OCT quantified by the FWHM value of the A-line signal; (c) lateral resolution of the SD-OCT quantified using the edge spread function; (d) lateral resolution of PAM quantified using the edge spread function.

launch the PA excitation laser pulse; the Gage card to acquire the PA signal; the NI acquisition card to acquire the OCT signal; and the customized motorized stage to scan. Therefore, the PAM and OCT imaging was performed simultaneously.

3. Results

The spatial resolution of the PAM-OCT system was quantified as shown in Fig. 2. The axial resolution was measured by imaging a 100 nm-thick homemade graphene film coated on a glass plate. The glass plate was placed under the prism, and a thin layer of DI water was used to fill the gap between the glass plate and the prism (as the coupling medium). To quantify the high frequency of this PAM, a digital oscilloscope (DPO 3034, Tektronix), with a super-high sampling rate of 2.5 GHz, was used to acquire the PA signal. Since the raw PA signal has a bipolar shape (having both positive and negative components), the axial resolution of the PAM was quantified *via* the shift-and-sum method [23,24]. Briefly, we first shifted the depth-resolved A-line signal of the homemade graphene film by a distance and added it to the original A-line signal. The smallest shifted distance that still allows resolution of the two peaks (by 10 % amplitude difference) was considered as the axial resolution and it was determined as 8 μm, as shown in Fig. 2(a).

Fig. 2(b) shows the axial resolution of SD-OCT taken by the FWHM of the original A-line signal, and it was determined as 7.6 μm. The lateral resolution of the PAM-OCT system was measured by imaging the sharp edge of a blade with a step of 2 μm. The results are shown in Fig. 2(c) and (d). The edge spread function (ESF) was calculated and then the line spread function (LSF) was simply the derivative of the ESF. We can see from the aforementioned results that the spatial resolutions of the dual modality system are well matched.

To demonstrate the complementary imaging capability of the PAM-OCT system, four human hairs (two black and two white) were embedded in scattering medium and imaged. The scattering medium was made of 97 % DI water, 2% agar and 1% intralipid solution. Fig. 3(a) and (b) show the maximum amplitude projected (MAP) and maximum intensity projected (MIP) images for OCT and PAM. The total data acquisition time was about 10 min and the field of view was 4 × 2.5 mm with step size of 5 μm. All four hairs were clearly imaged in OCT, but only the two black hairs appeared in the PAM image. This is because OCT is based on optical scattering, and both white and black hairs scatter light. In contrast, PAM only detects optical absorption, and the melanin in black hairs strongly absorbs much more light than white hairs. The black hairs in the PAM image are smaller than those in the OCT image. This is because the light wavelength of PAM is shorter than that of OCT and the lateral resolution of PAM is better than that of OCT. Fig. 3(c) and (d) are the B-scan images along the white dotted lines in Fig. 3(a) and (b), respectively. Because of the wide bandwidth of PAM and the strong light absorption of the black hair at 532 nm only allowing light to penetrate the very top surface, the hair cross section in the PAM result is not circular.

Next, we used this dual modality system to perform *in vivo* imaging of a nude mouse (~ 20 g). We first imaged the thin mouse ear. Then we imaged the hindlimb to demonstrate the ability to perform dual modality imaging that can only be performed in reflection mode. The mouse was first anesthetized by intraperitoneal injection of chloral hydrate solution at 0.1 mg/g. Then we fixed it on the motorized stage and raster-scanned its ear or hindlimb with a PAM laser of 800 nJ/pulse and OCT light of 2 mW. According to the ANSI laser safety standards, by calculation, the pulse energy cannot exceed 0.18 μJ and the pulse energy we used (800 nJ/pulse) was 4.4 times that value. However, the signal-to-noise ratio (SNR) was over 7.2, which means that we still could acquire signal above the noise level while remaining under the safety limit. The animal's body temperature was maintained with a heating pad. All animal procedures complied with protocols approved by the Institutional Animal Care and Use Committee of Peking University. The mouse recovered to its normal behavior condition after the experiments, and there was no observable damage to its ear or hindlimb.

Fig. 4 shows the dual modality imaging result of the mouse ear. Fig. 4(a) is the MIP result for OCT imaging. The total data acquisition time was about 10 min and the field of view was 3.0 × 2.25 mm with a step size of 5 μm. The blood vessels of the ear are faintly visible in the OCT image due to a strong optical scattering background. Fig. 4(b) is the MAP result for PAM imaging, where the blood vessels are clearly distinguished. Fig. 4(c) and (d) are the B-scan images along the white dotted line in Fig. 4(a) and (b). The OCT clearly differentiated the epidermis (ED), dermis (D), and cartilage (CT) while the PAM reconstructed the blood vessels with high contrast; the two images were fused in Fig. 4(e), demonstrating complementary tissue components with high spatial co-registration. It is worth noting that, owing to the superior high-axial resolution of PAM, even the cross sections of the smallest reconstructed vessels do not appear to be elongated in the axial direction. Two fly-through 3D animations of the fused dual modality image results are also available online (media 1 for the entire image, media 2 for the part of the image inside the white dotted rectangle in Fig. 4(b)).

Besides the thin mouse ear imaging, Fig. 5 shows the dual modality imaging results for the mouse hindlimb. The total data acquisition time was about 10 min and the field of view was 3.5 × 2.5 mm, with a step size of 5 μm. Fig. 5(a) is the MIP result for OCT imaging. The sebaceous glands (SG) are clearly visible due to strong optical scattering. Fig. 5(b) is the MAP result for PAM imaging, where the blood vessels are clearly distinguished. Fig. 5(c) and (d) are the B-scan images along the white dotted line in Fig. 5(a) and (b). The OCT clearly imaged the epidermis (ED), dermis (D), hypodermis (HD) and muscles (M) while the PAM reconstructed the blood vessels with high contrast. In Fig. 5(e), the fused B-scan image of Fig. 5(c) and (d), we can distinguish large and small blood vessels lying in different layers of D, HD, and M. For comparison, Fig. 5(f) shows the H&E-stained tissue sample of the hindlimb skin. Two fly-through 3D animations of the fused dual modality image results are also available online (media 3 for the entire image, media 4 for the part of the image inside the white dotted rectangle in Fig. 5(b)).

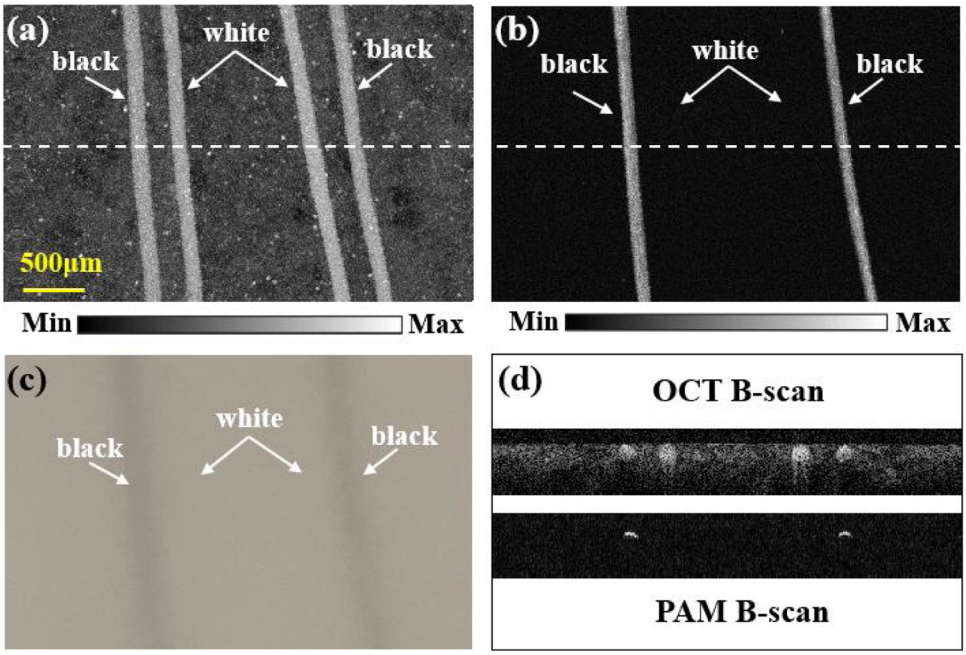

Fig. 3. Dual modality imaging of four human hairs embedded in a scattering medium. (a) OCT MIP imaging result; (b) PAM MAP imaging result; (c) Photograph of the phantom; (d) B-scan images along the white dotted line in (a) and (b) by OCT and PAM, respectively. Scale bar: 500 μm.

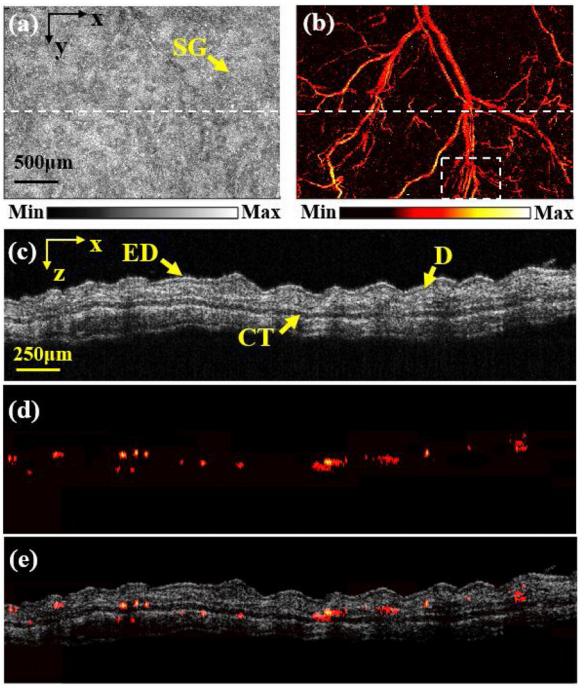

Fig. 4. Simultaneous *in vivo* imaging of a nude mouse ear. (a) OCT MIP image; (b) PAM MAP image; (c) B-scan image along the white dotted line in (a); (d) B-scan image along the white dotted line in (b); (e) fused B-scan image of the PAM-OCT system. SG, sebaceous gland; ED, epidermis; CT, cartilage; D, dermis. 3D visualizations of the fused image can be seen in **Visualization 1** and **Visualization 2**. Scale bar ((a), (b)): 500 μm; scale bar ((c), (d), (e)): 250 μm.

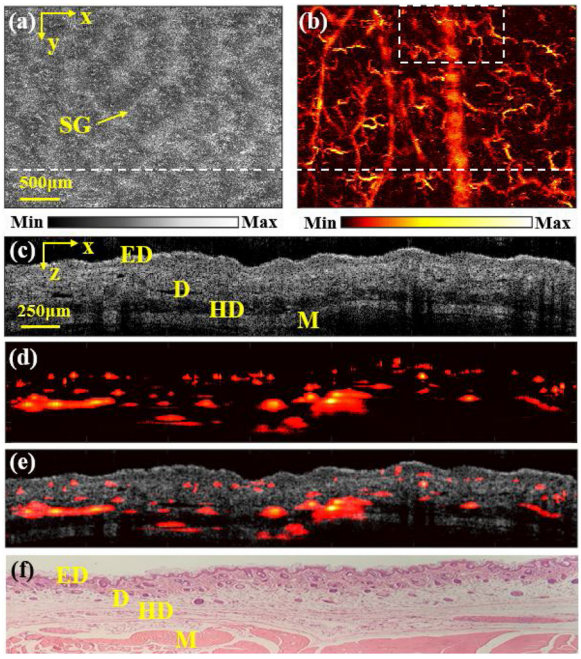

Fig. 5. Simultaneous *in vivo* imaging of a nude mouse hindlimb. (a) OCT MIP image; (b) PAM MAP image; (c) B-scan image along the white dotted line in (a); (d) B-scan image along the white dotted line in (b); (e) fused B-scan image of the dual modality PAM-OCT system; (f) Corresponding histology (H&E staining) of a nude mouse hindlimb. SG, sebaceous gland; ED, epidermis; D, dermis; HD, hypodermis; M, muscles. 3D visualizations of the fused image can be seen in **Visualization 3** and **Visualization 4**. Scale bar ((a), (b)): 500 μm; scale bar ((c), (d), (e), (f)): 250 μm.

4. Conclusions

In summary, an all-optically integrated resolution-matched reflection mode PAM-OCT system was successfully developed and tested. With the superior wide bandwidth of PAM, the axial resolutions of the PAM and OCT subsystems are well matched, which is important for accurate spatial co-registration of these two modalities. The capability to combine light scattering and absorb sample properties has been demonstrated through phantom imaging, and *in vivo* mouse ear and hindlimb imaging. In addition, the transparent characteristic of PRUD enables the dual modality system to work in reflection mode, which is ideal for *in vivo* biomedical imaging. Moreover, the current setup also has potential for integrating other optical imaging modes such as

fluorescent imaging and confocal microscopy to realize multi-modal *in vivo* imaging, which will be our future work. Therefore, this PAM-OCT system has an abundance of future applications in biomedical imaging.

Declaration of Competing Interest

We declare that we have no financial and personal relationships with other people or organizations that can inappropriately influence our work, there is no professional or other personal interest of any nature or kind in any product, service and/or company that could be construed as influencing the position presented in, or the review of, the manuscript entitled "Resolution-matched reflection mode photoacoustic microscopy and optical coherence tomography dual modality system".

Acknowledgments

The authors gratefully acknowledge support from the following grants: the National Key Research and Development Program from the Ministry of Science and Technology of the People's Republic of China (No. 2017YFE0104200), the National Natural Science Foundation of China (No. 81421004), and the National Key Instrumentation Development Project from the Ministry of Science and Technology of the People's Republic of China (No. 2013YQ030651). They also thank Dr. Zhaolong Chen and Prof. Zhongfan Liu for providing the graphene sheet.

Appendix A. Supplementary data

Supplementary material related to this article can be found, in the online version, at doi:https://doi.org/10.1016/j.pacs.2020.100188.

References

[1] C. Li, L.V. Wang, Photoacoustic tomography and sensing in biomedicine, Phys. Med. Biol. 54 (19) (2009) R59–97.
[2] D. Huang, et al., Optical Coherence Tomography Vol. 254 (1991), p. 1178.
[3] B. Zabihian, et al., In vivo dual-modality photoacoustic and optical coherence tomography imaging of human dermatological pathologies, Biomed. Opt. Express 6 (9) (2015) 3163–3178.
[4] C. Tian, et al., Noninvasive chorioretinal imaging in living rabbits using integrated photoacoustic microscopy and optical coherence tomography, Opt. Express 25 (14) (2017).
[5] V. Tsytsarev, et al., Photoacoustic and optical coherence tomography of epilepsy with high temporal and spatial resolution and dual optical contrasts, J. Neurosci. Methods 216 (2) (2013) 142–145.
[6] Y. Yang, et al., Integrated optical coherence tomography, ultrasound and photoacoustic imaging for ovarian tissue characterization, Biomed. Opt. Express 2 (9) (2011) 2551–2561.
[7] M. Liu, et al., Dual modality optical coherence and whole-body photoacoustic tomography imaging of chick embryos in multiple development stages, Biomed. Opt. Express 5 (9) (2014) 3150–3159.
[8] Q. Zhou, et al., Piezoelectric films for high frequency ultrasonic transducers in biomedical applications, Prog. Mater. Sci. 56 (2) (2011) 139–174.
[9] C. Zhang, et al., In vivo photoacoustic microscopy with 7.6-μm axial resolution using a commercial 125-MHz ultrasonic transducer, J. Biomed. Opt. 17 (2012) 116016.
[10] Z. Chen, et al., All-optically integrated photo-acoustic microscopy and optical coherence tomography based on a single Michelson detector, Opt. Lett. 40 (12) (2015) 2838–2841.
[11] T. Berer, et al., Multimodal noncontact photoacoustic and optical coherence tomography imaging using wavelength-division multiplexing, J. Biomed. Opt. 20 (4) (2015) 46013.
[12] S. Carp, et al., Optoacoustic imaging using interferometric measurement of surface displacement, Appl. Phys. Lett. 85 (2004) 5772–5774.
[13] J. Horstmann, et al., Full-field speckle interferometry for non-contact photoacoustic tomography, Phys. Med. Biol. 60 (2015) 4045–4058.
[14] T. Wang, et al., All-optical photoacoustic microscopy based on plasmonic detection of broadband ultrasound, Appl. Phys. Lett. 107 (2015) 153702.
[15] R. Haindl, et al., Dual modality reflection mode optical coherence and photoacoustic microscopy using an akinetic sensor, Opt. Lett. 42 (21) (2017).
[16] H. Li, et al., A transparent broadband ultrasonic detector based on an optical micro-ring resonator for photoacoustic microscopy, Sci. Rep. 4 (2014) 4496.
[17] F. Yang, et al., Broadband graphene-based photoacoustic microscopy with high sensitivity, Nanoscale 10 (18) (2018) 8606–8614.
[18] X. Zhu, et al., Ultrasonic detection based on polarization-dependent optical reflection, Opt. Lett. 42 (3) (2017) 439–441.
[19] E.Z. Zhang, et al., Multimodal photoacoustic and optical coherence tomography scanner using an all optical detection scheme for 3D morphological skin imaging, Biomed. Opt. Express 2 (8) (2011) 2202–2215.
[20] Y. Wang, C. Li, R.K. Wang, Noncontact photoacoustic imaging achieved by using a low-coherence interferometer as the acoustic detector, Opt. Lett. 36 (20) (2011) 3975–3977.
[21] C. Blatter, et al., Intrasweep phase-sensitive optical coherence tomography for noncontact optical photoacoustic imaging, Opt. Lett. 37 (21) (2012) 4368–4370.
[22] M. Wojtkowski, et al., Ultrahigh-resolution, high-speed, Fourier domain optical coherence tomography and methods for dispersion compensation, Opt. Express 12 (11) (2004) 2404–2422.
[23] Z. Xie, et al., Laser-scanning optical-resolution photoacoustic microscopy, Opt. Lett. 34 (2009) 1771–1773.
[24] G. Ku, et al., Photoacoustic microscopy with 2-microm transverse resolution, J. Biomed. Opt. 15 (2) (2010) 021302.

Xiaoyi Zhu received her B.S. degree in Biomedical Engineering from Chongqing University in 2010 and Ph.D. degree in Biomedical Engineering from Peking University in 2019. Now, she is a post doctor in Duke University. Her interest focuses on photoacoustic imaging, multimodal imaging and fast scanning imaging system.

Zhiyu Huang is Ph.D. student at Peking University, Department of Biomedical Engineering, College of Engineering. He received his bachelor's degree in applied mathematics from Xidian University. His research focuses on the optimization and image processing of OCT systems.

Ziyuan Li is a Ph.D. student of Department of Biomedical Engineering in Peking University. He received his bachelor's degree in pharmacy form Peking University in 2016. Also, he received his Master degree in pharmaceutics form Peking University in 2018. Research interest: Development of multimodal probe synthesis and imaging techniques for diagnosis.

Wenzhao Li is an electronic engineer working in the Department of Biomedical Engineering, School of Engineering, Peking University. His research focuses on analog electronic circuits, signal measurement, and embedded system design.

Dr. Xi Liu is a graduated Ph.D. student from Peking University, Department of Biomedical Engineering. His research focuses on Optical Coherence Tomography.

Zhaolong Chen is a Ph.D. student at Peking University. He received his B.S. in chemistry from Shandong University in 2014. His current research is focused on controlled growth of graphene on glass and sapphire substrates by the CVD method and its applications in light-emitting diodes.

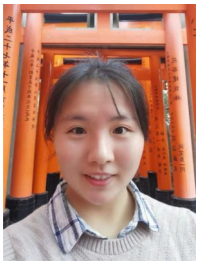

Jian Tian got her Ph.D. degree from biomedical engineering in Peking University and prepared to work in Center for Medical Device Evaluation of NMPA. Her research interest focuses on molecular imaging, especially on PET/CT image quality assessment, automatic lesion segmentation and cost-effectiveness analysis. In the future, she will pay more attention on regulatory affairs.

Changhui Li is an associate professor in the department of Biomedical Engineering of Peking University. He received his B.Sc. degree in 1997 from Peking University and Ph.D. degree in 2006 from Texas A&M University. Prior to joining Peking University, he worked at Washington University, St. Louis as a post doctor from 2006 to 2010. His research focuses on developing novel biomedical imaging methods, including photoacoustic imaging and fluorescence imaging.